Prospects of Searches for the Higgs Boson at the LHC

Bruce Mellado

Physics Department, University of Wisconsin - Madison, Madison, Wisconsin 53706, USA

One of the most exciting prospects for the Large Hadron Collider is to observe the Higgs boson. The most important experimental characteristics of the two general-purpose detectors, the CMS and ATLAS experiments are summarised. The sensitivity for the CMS and ATLAS experiments at the LHC to discover a Standard Model Higgs boson with relatively low integrated luminosity per experiment is outlined. The most relevant discovery modes are covered. A brief discussion about the expected performance from these experiments in searches for one or more of the Higgs bosons from the minimal version of the supersymmetric theories is also included.

1. Introduction

In the Standard Model (SM) of electroweak and strong interactions, there are four types of gauge vector bosons (gluon, photon, W and Z) and twelve types of fermions (six quarks and six leptons) [1–4]. These particles have been observed experimentally. At present, all the data obtained from the many experiments in particle physics are in agreement with the SM. In the SM, there is one particle the Higgs boson, that is responsible for giving masses to all the particles [5–10]. In this sense, the Higgs particle occupies a unique position.

Prior to the end of the year 2000, the Higgs particle was not observed experimentally. After the centre-of-mass energy at the LEP[1] accelerator of CERN reached 205 GeV/c^2 in 2000, excess candidates began to show up in the SM Higgs boson analysis in the ALEPH experiment, consistent with a Higgs boson mass, M_H, around 115 GeV/c^2 [11, 12]. One of the most exciting prospects for the Large Hadron Collider (LHC) [13] is confirming or rejecting the first possible experimental evidence for the Higgs particle at a mass around 115 GeV/c^2.

The Higgs boson mass is not predicated by theory and, to date, direct experimental searches for the Higgs boson have put a lower limit on its mass at $M_H > 114.4$ GeV/c^2 @ 95% confidence level (CL) [12, 14].[2] Figure 1 shows the $\Delta\chi^2$ curve derived from high-Q^2 precision electroweak measurements, performed at LEP and by SLD, CDF and D0, as a function of the Higgs boson mass, assuming the SM. While this is not a proof that the SM Higgs boson actually exists, it does serve as a guideline in what mass range to look for it. A preferred value for the Higgs boson mass, derived by fitting precision electroweak data [15] is currently $M_H = 84^{+34}_{-26}$ GeV/c^2 with an upper bound of 154 GeV/c^2 @ 95% CL.

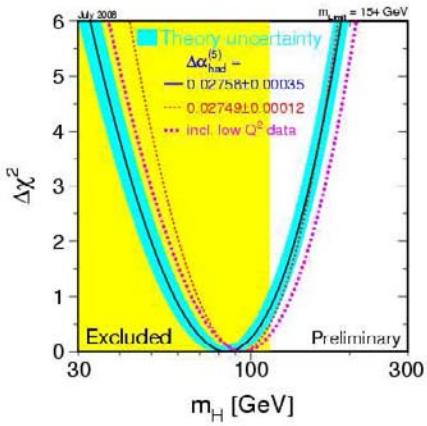

Figure 1. $\Delta\chi^2$ curve derived from high-Q^2 precision electroweak measurements, performed at LEP and by SLD, CDF and D0, as a function of the Higgs boson mass

Both the CMS and ATLAS experiments at the LHC, scheduled for proton-proton collision data-taking in 2009, have been designed to search for the Higgs boson over a wide mass range [16, 17]. The CMS and ATLAS detectors were designed for the search for the Higgs boson using, for the most part, inclusive signatures. In recent years significant progress has been made, both in the phenomenology and experimentally, in demonstrating the feasibility of observing a low mass SM Higgs boson in association with jets using different decay modes [16, 18–25].[3] Here we summarise the

[1] LEP stands for Large Electron-Positron Collider.

[2] This is usually referred to as the LEP limit.

[3] The search for a heavy SM Higgs boson in association with high transverse momentum hadronic jets had been considered earlier [26].

sensitivity for each experiment to discover a SM Higgs boson with relatively low integrated luminosity per experiment (1–30 fb^{-1}) as well as recent developments that have enhanced this sensitivity.

In this paper we briefly review the experimental apparatus, covering the most relevant parameters of the LHC accelerator facility (Section 2.1) together with the CMS and ATLAS detectors (Sections 2.2 and 2.3). In section 3 we'll touch upon the production mechanisms, of the Higgs boson in proton-proton collisions with the most important discovery modes and related experimental aspects. Section 4 summarises the discovery potential of the CMS and ATLAS detectors.

2. The Experimental Apparatus

2.1. The Large Hadron Collider

The LHC [13] at the European Organisation for Nuclear Research (CERN) is a two-ring-superconducting hadron accelerator collider constructed in the already existing 26.7 km tunnel that was used for the LEP machine. The LHC displays high luminosity experiments, CMS [27] and ATLAS [28], both aiming at registering proton-proton collisions with a peak instantaneous luminosity of $L = 10^{34}$ cm^{-2}s^{-1}. There are also two low luminosity experiments: LHCb [29][4] for B-physics, aiming at a peak instantaneous luminosity of $L = 10^{34}$ cm^{-2}s^{-1}, and TOTEM [30] for the detection of protons from elastic scattering at small angles, aiming at a peak instantaneous luminosity of $L = 10^{29}$ cm^{-2}s^{-1}. In addition to the proton beams, the LHC will also be operated with ion beams. The LHC has one dedicated ion experiment, ALICE [31],[5] aiming at a peak instantaneous luminosity of $L = 10^{27}$ cm^{-2}s^{-1} for nominal lead-lead ion operation.

To collide two counter-rotating proton beams requires opposite magnetic dipole fields in both rings. The LHC is designed as a proton-proton collider with separate magnet fields and vacuum chambers in the main trajectories and with common sections only at the insertion regions where the detectors are located. The two beams share an approximately 130 m long beampipe along the interacting regions. According to the design, a large number of bunches (2808 for each proton beam) will be provided with a nominal bunch spacing of 25 ns. The long common beam pipe implies 34 parasitic collision points at each insertion region where the detectors will observe collisions. The LHC uses twin bore magnets since there is not enough room for two separate rings. These consist of two sets of coils and beam channels within the same mechanical structure and cryostat. The peak beam energy depends on the integrated dipole field around the storage ring. This implies a peak dipole field of 8.33 T for the 7 TeV in the LHC machine and the use of superconducting magnets.

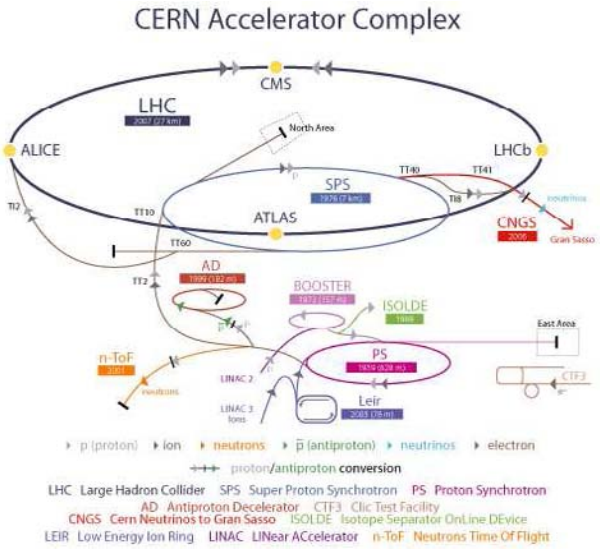

Figure 2. The LHC accelerator complex. CERN's accelerator complex is a succession of particle accelerators that can reach increasingly higher energies. Each accelerator boosts the speed of a beam of particles, before injecting it into the next one in the sequence

CERN's accelerator complex is a succession of particle accelerators that can reach increasingly higher energies (Fig. 2). Each accelerator boosts the speed of particles clustered in bunches, before injecting it into the next one in the sequence. Protons are produced by ripping off electrons from hydrogen atoms. They are injected from the linear accelerator (LINAC2) into the PS booster, then into the Proton Synchrotron (PS), followed by the Super Proton Synchrotron (SPS). Finally, the protons reach the LHC. Protons will circulate in the LHC for 20 minutes before reaching the maximum speed and energy.

2.2. The CMS Experiment

The Compact Muon Solenoid (CMS) is one of two general-purpose experiments at the LHC designed to explore the physics at the energy frontier [27]. The main volume of the CMS detector (Fig. 3) is a multilayered cylinder, about 21.3 m long and 16 m in diameter, weighing more than 13,000 tons. The innermost

[4] LHCb stands for Large Hadron Collider Beauty Experiment.
[5] ALICE stands for A Large Ion Collider Experiment.

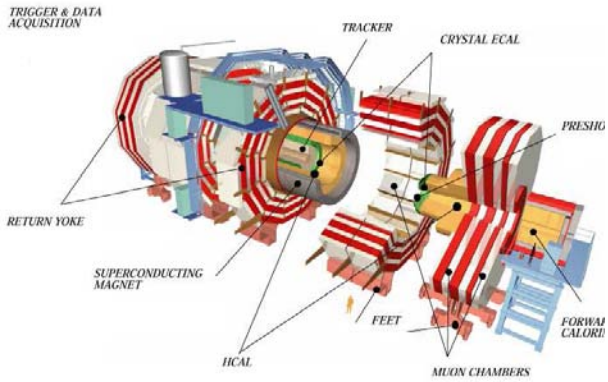

Figure 3. The CMS detector

layer is a silicon-based particle tracker, surrounded by electro-magnetic and hadronic calorimeters for measuring particle energies. These detector devices are placed inside a central superconducting solenoid magnet, 13 m long and 6 m in diameter. The magnetic field produced by the superconducting solenoid is used to measure the momentum of particles. Outer muon detectors surround the central magnet. The CMS detector is a hermetic detector in the range $|\eta| < 5$.

2.2.1. The Inner Tracker

The inner tracking system of CMS is designed to give a precise measurement of the trajectories of charged particles coming out from the LHC collisions [27]. Secondary vertexes will be reconstructed precisely, as well. The Inner Tracker surrounds the interaction point and has a length of 5.8 m and a diameter of 2.5 m. The CMS solenoid provides a homogeneous magnetic field of 4 T over the full volume of the Inner Tracker. The tracker is entirely based on silicon detectors due to the requirements of granularity, occupancy, speed and radiation hardness. The CMS Inner Tracker is composed of a pixel detector with three barrel layers at radii between 4.4 cm and 10.2 cm and a silicon strip tracker with 10 barrel detection layers to a radius of 1.1 m. Each system is covered on backward and forward sides by end-caps which consist of two disks in the pixel detector and three plus nine disks in the strip tracker on each side of the barrel, extending the acceptance of the tracker up to a pseudorapidity of $|\eta| < 2.5$.[6] The CMS Inner Tracker, with about 200 m^2 of active silicon are, is the largest silicon tracker ever assembled. In addition, CMS is the first experiment using silicon detectors in this outer tracker region. The construction of the CMS tracker, composed of 1440 pixel and 15,148 strip detector modules, required the development of production methods and quality control procedures that are new to the field of particle physics detectors.

In order to keep the occupancy at or below 1%. pixelated detectors with radii below 10 cm need to be constructed. The pixel size is 100×150 μmm in $-\phi$ and z, respectively. This is driven by the impact parameter resolution. In this configuration the occupancy is of the order 10^{-4} per pixel and the LHC bunch crossing. At intermediate radii (20 cm $<$ $<$ 55 cm) the reduced particle flux allows the use of silicon micro-strip detectors with a typical cell size of 10 cm $\times$ 80 μm. This results in an expected occupancy of up to $2 \div 3\%$ per strip and the LHC bunch crossing.

In order to maintain a good signal to noise ratio well above 10, CMS uses thicker silicon sensors for the outer tracker region (500 mm thickness as opposed to the 320 mm in the Inner Tracker) with correspondingly higher signal. Cell sizes up to about 25 cm $\times$ 180 μm can be used in the outer region of the tracker, with an occupancy of about 1%.

2.2.2. The Calorimeter

One of the driving criteria in the design was the capability to detect two photons coming from the decay of a Higgs boson (Section 3). This capability is enhanced by the good energy resolution provided by a homogeneous crystal calorimeter. The use of high density crystals has allowed the design of a calorimeter which is fast, has fine granularity and is radiation resistant, all important characteristics in the LHC environment.

The electro-magnetic calorimeter of CMS (ECAL) is a hermetic homogeneous calorimeter consisting of 61,200 lead tungstate ($PbWO_4$) crystals mounted in the central barrel part [27]. The barrel part is closed by 7324 crystals in each of the two end-caps. Avalanche photo-diodes are used as photo-detectors in the barrel and vacuum photo-triodes in the end-caps. A preshower detector is placed in front of the end-cap crystals.

The barrel part of the ECAL (EB) covers the pseudorapidity range $|\eta| < 1.479$. The barrel granularity is 360-fold in ϕ and 2×85-fold in η, resulting in a total of 61,200 crystals. The crystals have a tapered shape, slightly varying with position in η. They are mounted in a quasi-projective geometry to avoid cracks aligned with particle trajectories, so that their axes make a small angle (3^o) with respect to the vector from the nominal interaction vertex, in both the ϕ and η projec-

[6] Pseudorapidity, η, is defined as $\eta = -\log(\tan(\theta/2))$, where, θ is the polar angle.

tions. The crystal cross-section corresponds to approximately 0.0174×0.0174 in $\eta \times \phi$ or 22×22 mm^2 at the front face of crystal, and 26×26 mm^2 at the rear face. The crystal length is 230 mm corresponding to $25.8\,X_0$.

The end-caps (EE) cover the range $1.479 < |\eta| < 3.0$ [27]. The distance between the interaction point and the end-cap envelope is 315.4 cm. The end-cap consists of identically shaped crystals grouped in mechanical units of 5×5 crystals (super-crystals, or SCs) consisting of a carbon-fiber alveolar structure. The crystals and SCs are arranged in a rectangular x–y grid, with the crystals pointing at a focus 1300 mm beyond the interaction point, giving off-pointing angles ranging from 2–8 degrees. The crystals have a rear face cross section 30×30 mm^2, a front face cross section of 28.62×28.62 mm^2 and a length of 220 mm ($24.7\,X_0$).

The hadronic barrel calorimeter (HB) is a sampling calorimeter covering the range $|\eta| < 1.3$ consisting of 36 identical azimuthal wedges arranged in two half-barrels [27]. The wedges are constructed out of flat brass absorber plates aligned parallel to the beam axis. The plastic scintillator is divided into 16 η sectors, resulting in a segmentation $\Delta\eta \times \Delta\phi = 0.087 \times 0.087$. The total absorber thickness at 90^o is 5.82 interaction lengths, λ. The HB effective thickness increases with polar angle (θ) as $1/\sin\theta$, resulting in 10.6 λat $|\eta| < 1.479$. The electro-magnetic crystal calorimeter in front of HB adds about 1.1 λ of material. In the central pseudorapidity region, the combined stopping power of EB plus HB does not provide sufficient containment for hadron showers. To ensure adequate sampling depth for $|\eta| < 1.3$, the hadron calorimeter is extended outside the solenoid with a tail catcher called the outer calorimeter.

The hadron calorimeter end-caps (HE) cover $1.3 < |\eta| < 3$ and it is a sampling calorimeter [27]. The total length of the calorimeter, including electro-magnetic crystals, is about $10\,\lambda$. Quartz fibers were chosen as the active medium for the forward calorimeter, extending the calorimeter coverage to $|\eta| < 5$ [27]. The calorimeter consists of a steel absorber structure that is composed of 5 mm thick grooved plates and fibers are inserted in these grooves.

2.2.3. The Muon System

CMS uses three different types of gaseous particle detectors for muon identification [27]. In the barrel region the neutron-induced background and the muon rate are low. Here the $\int Bdl$ is uniform and mostly contained in the steel yoke. Standard rectangular drift chambers are used, which are outside the cryostat. The barrel drift tube (DT) chambers cover the range $|\eta| < 1.2$. In the two end-cap regions the muon rates and background levels are high and the magnetic field is large and non-uniform. Here the muon system consists of cathode strip chambers (CSC). With their fast response time, fine segmentation and radiation resistance, the CSCs identify muons in the range $0.9 < |\eta| < 2.4$. A complementary, dedicated trigger system consisting of resistive plate chambers (RPC) was added. The RPCs are assembled in both the barrel and end-cap regions. The RPCs provide a fast, independent and highly segmented trigger with a sharp transverse momentum threshold over a large portion of the rapidity range $|\eta| < 1.6$.

2.2.4. The Superconducting Magnet

The superconducting magnet for CMS was designed to produce a 4-T magnetic field in a free bore of 6 m diameter and 12.5 m length with a total stored energy of 2.6 GJ at full current [27]. The return flux occurs through a 10000-t yoke comprising 5 wheels and 2 end-caps, composed of three disks each. The distinctive feature of the 220-tonne cold mass is the 4-layer winding made from a stabilised reinforced NbTi conductor. The ratio between stored energy and cold mass is high (11.6 KJ/kg), causing a large mechanical deformation (0.15%) during energising. This is well beyond the values of previous solenoidal detector magnets. The magnet was designed to be assembled and tested in a surface hall (SX5), prior to being lowered 90 m below ground to its final position in the experimental cavern. After provisional connection to its ancillaries, the CMS magnet has been fully and successfully tested and commissioned in SX5 during the autumn 2006.

2.2.5. The Trigger and Data Acquisition Systems

In order to reduce the GHz proton-proton collision rate expected at design instantaneous luminosity, the CMS detector pursues a two-level trigger system: Level-1 (L1) trigger and High-Level Trigger (HLT), respectively [27]. The L1 trigger consists of custom-designed, largely programmable electronics, whereas the HLT is a software system implemented in a filter farm of about 1000 commercial processors. The rate reduction capability is designed to be at least a factor of 10^6 for the combined L1 trigger and HLT. The design output rate limit of the L1 trigger is 100 kHz. The L1 trigger uses coarsely segmented data from the calorimeters and the muon system, while holding the high resolution data in pipelined memories in the front-end electronics. The HLT has access to the complete read-out data and can therefore perform complex calculations similar to those

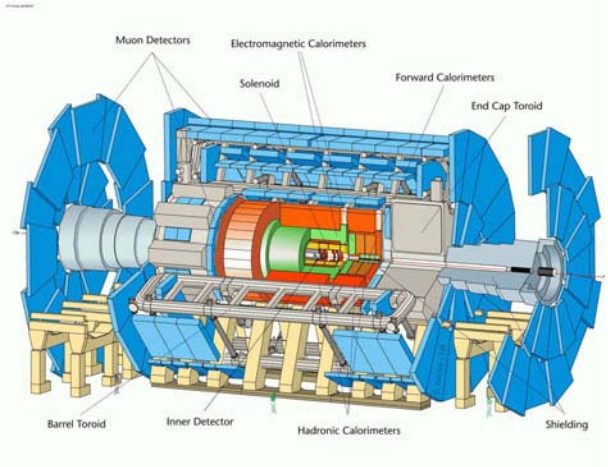

Figure 4. The ATLAS detector

made by the analysis off-line software if required for specially interesting events. The Global Calorimeter and Global Muon Triggers determine the highest-rank calorimeter and muon objects across the entire experiment and transfer them to the Global Trigger. The latter takes the decision to reject an event or to accept it for further evaluation by the HLT. The output rate of the HLT is 200 Hz. The CMS Data Acquisition System is designed to handle the data flow driven by the trigger chain.

2.3. The ATLAS Experiment

ATLAS (A Toroidal LHC ApparatuS) is one of the two general-purpose experiments at the LHC designed to explore the physics at the energy frontier [28]. The ATLAS detector consists of four major components, the Inner Tracker which measures the momentum of each charged particle, the calorimeter which measures the energies carried by the particles, the muon spectrometer which identifies and measures muons and the magnet system that bends charged particles for momentum measurement (Fig. 4). The detector is a cylinder with a total length of 42 m and a radius of 11 m and weighs approximately 7000 tonnes. The ATLAS detector is hermetic in the range $|\eta| < 4.9$.

2.3.1. The Inner Tracker

The ATLAS Inner Tracker provides precise measurement of the trajectories of charged particles that pass through the region in the range $|\eta| < 2.5$ [28]. The innermost layer is a precision tracker comprised of three layers of silicon pixel detectors, arranged in a cylindrical geometry, with an inner radius of about 50 mm, an outer radius of about 150 mm and a total length of about 1.3 m. It provides position measurements with an accuracy of about 10 μm in R–ϕ and about 115 μm in z in the barrel, with similar precision for the disks at either end.

The middle layer, the Semiconductor Tracker (SCT), uses four stereo layers of silicon strip detectors with one set of strips in each layer offset by a small angle with respect to the other, to provide additional position measurements with a precision of 17 μm in R–ϕ and about 580 μm in z, again with similar precision for the disks at either end. The SCT has an inner radius of about 250 mm, an outer radius of about 600 mm, and a length of about 5.4 m.

The outer layer, the Transition Radiation Tracker (TRT), is a straw tube tracker that provides a large number (about 36 per track) of R–ϕ measurements in the region with radius, R, from about 550 mm to about 1100 mm. The straws are interleaved with polypropylene (fibers in the barrel region, foil in the end-caps) to provide transition radiation to help with electron identification. The total length of the TRT is about 5.4 m; this corresponds to the range $|\eta| < 2.5$. The precision of the R–ϕ measurement is 130 μm per straw.

The material budget of the ATLAS Inner Detector ranges from < 0.5 radiation lengths and 0.2 interaction lengths near $\eta = 0$ to almost 2.5 X_0 and 0.7 λ in the region around $|\eta| = 1.6$–1.7. This large material budget can lead to degraded performance for the reconstruction of physics objects.

2.3.2. The Calorimeter

The innermost layer, comprised of the Liquid Argon (LAr) barrel and end-cap electromagnetic calorimeters, is a lead-LAr detector with accordion-shaped absorbers and electrodes [28]. This unusual geometry is intended to improve the readout time of the detector by avoiding current loops. It has a thickness > 22 X_0 in the barrel region and a thickness > 24 X_0 in the end-cap. The electromagnetic calorimeters are arranged in three layers, plus a pre-sampler in the region $|\eta| < 1.8$. The granularity of the pre-sampler in $\eta \times \phi$ is 0.025×0.1. The first sampling is segmented into strips of $\eta \times \phi$ is $0.025/8 \times 0.1$ in the range $|\eta| < 1.4$; the granularity decreases in the forward regions. Similarly, the second sampling has a granularity of 0.025×0.025 in $|\eta| < 1.4$, with similar or lower granularity in other regions. Finally, the third sampling is segmented into cells of 0.05×0.025 in $|\eta| < 1.35$ and in the range $1.5 < |\eta| < 2.5$.

The Tile Calorimeter (TileCal), placed directly outside the LAr calorimeter, is a hadronic sampling

calorimeter using steel as the absorber and scintillating tiles as the active material [28]. It is separated into two regions, the barrel region with $|\eta| < 1$ and the extended barrel region with $0.8 < |\eta| < 1.7$. Like the electromagnetic calorimeter, the tile calorimeter is segmented longitudinally into three layers. In the barrel, the first layer has a thickness of about 1.5 λ, the second about 4.1 λ, and the thickness of the third sampling is 1.8 λ. In the extended barrel, these figures are 1.5 λ, 2.6 λ and 3.3 λ, respectively. The granularity of the first two layers of the tile calorimeter is 0.1×0.1; the granularity of the last layer is 0.1×0.2.

In the region $|\eta| > 1.5$ liquid argon is used as the active medium for the hadronic calorimetry. The Hadronic End Cap (HEC) uses copper plates as the absorber and covers the range up to $|\eta| < 3.2$ to a depth of about 10 λ [28]. It has three layers, with a granularity of 0.1×0.1 in the range $|\eta| < 2.5$ and 0.2×0.2 in the range $|\eta| > 2.5$.

The forward calorimeter (FCal) covers the region with $3.1 < |\eta| < 4.9$; like the other calorimeters, it is also divided into three longitudinal layers [28]. The FCal is split into one electromagnetic calorimeter and two hadronic calorimeters, each about 45 cm deep. The absorber for the electromagnetic FCal is copper; for the hadronic FCal modules, it is tungsten. The granularity is dependent on η and it is slightly different for the three different FCal modules, but in general it is lower for the FCal than for the other calorimeters.

2.3.3. The Muon System

The muon spectrometer consists of a large air-core toroidal magnet system instrumented with a variety of detectors that provide position measurements for muon tracks passing through its volume. The toroidal magnetic field geometry was chosen so that the momentum resolution will not be degraded significantly in the forward directions. Muon trajectories are measured by three concentric cylindrical shells of detectors with radii of about 5, 7.5 and 10 m in the barrel region, and by four end-cap "wheels" located at $|z| \approx$7.4, 10.8, 14 and 21.5 m. The Monitored Drift Tubes (MDTs) are aluminum tubes with a diameter of about 30 mm; they are filled with a gas mixture of 93% argon and 7% of CO_2, with a tungsten-rhenium wire running down the centre [28]. Each MDT chamber provides a measurement of the bending direction, z (in the barrel) or R (in the end-cap), with precision of approximately 34 μm. The MDTs cover the full range of $|\eta| < 2.7$, except for the first layer which only covers $|\eta| < 2$.

Cathode Strip Chambers (CSCs) consist of thin anode wires suspended halfway between two parallel plates covered with cathode strips, with one layer oriented parallel to the wires and the other perpendicular; position measurements (in both the bending and azimuthal directions) are taken from these cathode strips and not the anode wires [28]. Four wire planes per chamber provide position measurements with a precision of about 60 μm per CSC plane in the bending direction and about 0.5 cm in the azimuthal direction

In addition to the MDTs and the CSCs ATLAS displays two muon subsystems used for triggering on muons candidates. Resistive Plate Chambers (RPCs) cover the region with $|\eta| < 1.05$ [28]. RPCs are parallel-plate electrodes filled with a gaseous mixture. Thin Gap Chambers (TGCs) cover the region with $1.05 < |\eta| < 2.4$ [28]. These are multi-wire proportional chambers similar to the CSCs.

2.3.4. The Magnet System

The central ATLAS solenoid has a length of 5.3 m with a bore of 2.4 m. The conductor is a composite that consists of a flat superconducting cable located in the centre of an aluminum stabiliser with rectangular cross-section. It is designed to provide a field of 2 T in the central tracking volume with a peak magnetic field of 2.6 T. To reduce the material build-up the solenoid shares the cryostat with the Liquid Argon calorimeter.

The ATLAS toroid magnet system consists of eight barrel coils housed in separate cryostats and two End-Cap cryostats housing eight coils each. The End-Cap coils systems are rotated by 22.5^o with respect to the barrel toroids in order to provide radial overlap and to optimize the bending power in the interface regions of both coil systems.

2.3.5. The Trigger and Data Acquisition Systems

The ATLAS trigger consists of a three-level system: the first-level trigger or Level-1, the second-level trigger or Level-2 and the third-level trigger or the Event Filter (EF) [32, 33]. Event selection is performed at Level-2 and EF with software algorithms. Both triggers have strong similarities in terms of software frameworks and architecture. They are commonly referred to as the High Level Trigger (HLT). The Level-1 trigger [32] reduces the initial 40 MHz to $<$ 75 kHz in $<$ 2.5 μs, the maximum output rate and latency the trigger hardware can tolerate. In the HLT [33], where the boundary between the two trigger steps is purposefully kept flexible, the Level-2 trigger will reduce the rate to O(2) kHz and the EF further to O(200) Hz. The available average latency of the two steps is substantially different, with $\sim$ 10 ms for the Level-2 trigger and $\sim$ 1 s for the EF.

The ATLAS Data Acquisition System is designed to handle the data flow driven by the trigger chain.

3. The Search for the Higgs Boson

In this section we deal with the most relevant aspects that define the different experimental analyses. In section 3.1 a brief overview of the production mechanisms and decay mode is given. In section 3.2 we give a brief overview of the experimental reconstruction of physics objects relevant to Higgs boson searches. In section 3.3 we give the specifics of the most relevant analysis for the observation of the Higgs boson.

3.1. Production Mechanisms and Decay Modes

When it comes to defining the experimental strategy for searches of the Higgs boson several theoretical inputs are necessary: the Higgs boson width, decay products and production mechanisms. The CMS and ATLAS detectors have been designed to a significant degree according to these theoretical inputs and within the context of inclusive analyses. A very important theoretical input is the expected natural width of the Higgs boson. Figure 5 shows the total width of the SM Higgs boson as a function of the mass [34]. In the mass range that seems to be preferred by the electroweak constraints (Section 1) the SM Higgs boson width is well below a GeV/c^2. For masses close to the LEP limit, the SM Higgs boson width is expected to be of the order of (1) MeV/c^2, which is much smaller than the resolutions that can be achieved experimentally. As a result, for practical purposes the width of the low mass SM Higgs boson is neglected in experimental searches. The SM Higgs boson natural width becomes comparable to the experimental resolution in some of the discovery channels (Section 3.3) for $M_H > 250 \div 300$ GeV/c^2. The SM Higgs boson width grows rapidly with the mass and at some point reaches (10^2) GeV/c^2, making experimental observation more challenging. On the other hand, when at the SM Higgs boson mass approaches TeV/c^2 perturbation theory breaks down and some of the theoretical inputs used here are not valid anymore.

Figure 6 shows the branching ratios of the SM Higgs boson to different decay products [34]. Branching ratios in Fig. 6 are given as a function of the Higgs boson mass. The final states most suitable for discovery at the LHC vary depending on the branching ratios, which are a function of the Higgs boson mass, and the relevant backgrounds. For $M_H < 2M_W$ the dominant decay mode is through $b\bar{b}$. However, due to the enormous QCD background, this channel is only considered in the $t\bar{t}H$ final state where handles exist for the rejection of this background.[7] The $\gamma\gamma$ final state, which appears when the Higgs boson decays via bottom, top and W loops, has a small branching fraction but excellent γ/jet separation and γ resolution help to make this a very significant channel. The $H \to \tau\tau$ decay is accessible if the Higgs boson is produced in association with jets (Section 3.3).

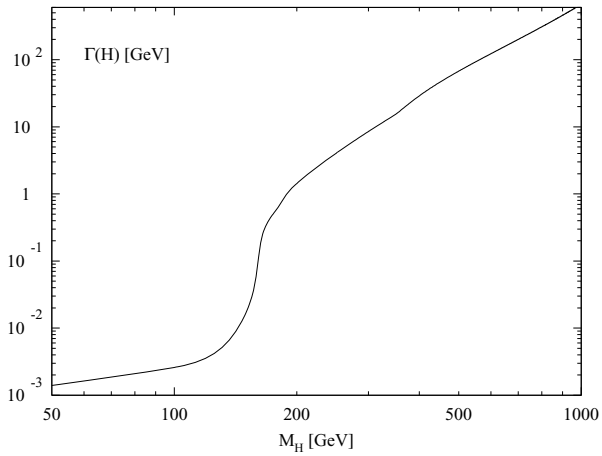

Figure 5. Total width of the SM Higgs boson to different decay products as a function of the mass

If the Higgs boson mass is large enough to make the WW and ZZ modes kinematically accessible, the $H \to WW^{(*)}$ final-states are powerful over a very large mass range (WW accounts for ∼95% of the branching ratio at M_H ∼160GeV/c^2), as is the $H \to ZZ^{(*)} \to 4l$ final state–the latter of which is commonly referred to as the "Golden Mode" as with four leptons in the final state the signal is easy to trigger on and allows for full reconstruction of the Higgs boson mass.

For SM Higgs boson masses close to $2m_{top}$, the channel $H \to t\bar{t}$ opens up, thus reducing the branching ratio of $H \to ZZ, WW$. Due to the very large cross-section for the production of non-resonant $t\bar{t}$ pairs, the inclusive search for the SM Higgs boson with $H \to t\bar{t}$ is not considered feasible.

The SM Higgs boson will be produced at the LHC via several mechanisms. The Higgs boson will be predominantly produced via gluon-gluon fusion [35] (see the left diagram in Fig. 7). For Higgs boson masses, such that $M_H > 100$ GeV/c^2, the second dominant process is the Vector Boson fusion (VBF) [36, 37] (see right diagram

[7] The observation of a Higgs boson with the $b\bar{b}$ decay in association with $t\bar{t}$ is not considered here as a discovery channel for the SM Higgs boson.

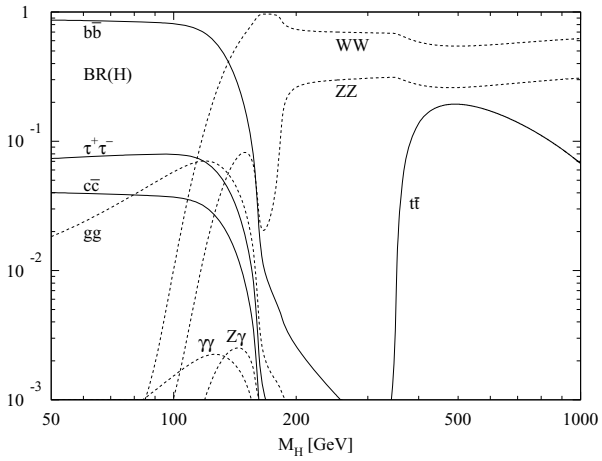

Figure 6. Branching ratio of the SM Higgs boson to different decay products as a function of the mass

in Fig. 7).

In addition to inclusive searches, the CMS and ATLAS collaboration have investigated the feasibility of observing the Higgs boson in association with at least one or two high transverse momentum, p_T, hadronic jets. In the case of gluon-gluon fusion the Higgs boson can be produced alone. However, when one of the gluons or top quarks emits a gluon, the Higgs boson is produced with the gluon, which is seen in the detector as a hadronic jet. When the Higgs boson has a significant transverse momentum the associated jet tends to be back-to-back with the Higgs boson in the transverse plane (for reasons of transverse momentum balance). In the case of VBF the Higgs boson is produced with at least two jets. In both cases, jets produced in association with the Higgs boson are most useful in the identification of the Higgs boson, suppressing significantly the QCD backgrounds. The presence of one or two high p_T hadronic jets in association with the Higgs boson produces two distinct type of topologies. The hadronic jet in final states with one jet tends to be more forward and the invariant mass of the Higgs boson system and the jet tend to be larger than that of the backgrounds [20,24,25]. These and other particular properties are used to suppress backgrounds.

In events with two high p_T jets produced by the VBF process display different peculiarities. The VBF process gives final state in which the two struck quarks appear as high-p_T jets in the forward (high-η) and opposite regions of the detectors (backward-forward). In addition,

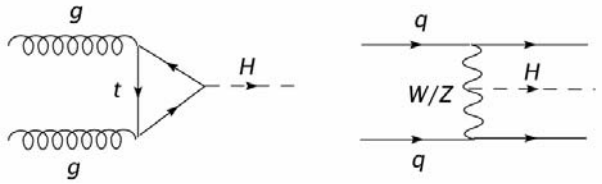

Figure 7. Leading order diagrams for the dominant processes involving the production of a SM Higgs boson at the LHC: gluon-gluon fusion (left) and VBF (right)

due to the lack of QCD colour flow between the scattered quarks, low hadronic activity is expected to arise, giving rise to a final state with a depleted hadronic activity. The application of a central jet veto, in addition to the presence of two forward high p_T jets in opposite hemispheres and a cut on the invariant mass of the di-jet system reduces QCD backgrounds very strongly and enhances significantly the sensitivity of searches for a low mass Higgs boson at the LHC [18–22].

Early analyses performed at the parton level associated with one or two high transverse momentum hadronic jets indicated that this final state can be a powerful observation mode for a low mass Higgs. The ATLAS and CMS collaborations have performed feasibility studies for SM Higgs boson searches in association with two jets including more detailed detector description and the implementation of initial state and final state parton showers, hadronisation and multiple interactions, which has confirmed the strong potential of these final states [16, 23].

The SM Higgs boson production cross-sections at the LHC to QCD Next-to-Leading-Order (NLO) [38–42],[8] as a function of Higgs boson mass are shown in Fig. 8[9] fusion mode. The Higgs boson cross-section with this mechanism reaches over 30 pb for masses around 115 GeV/c^2. The VBF process is the second most dominant production mode at the LHC. It typically takes up $\approx 10\%$ of the total Higgs boson cross-section for low masses and up to $\approx 50\%$ for a very heavy Higgs boson. Associated production modes, where the Higgs boson is produced via $^{-\prime} \to HW$, $^{-} \to HZ$ and gg, $^{-} \to t\bar{t}H$, have smaller cross-sections. The presence of a W, Z or

[8] The references given here correspond to the first computations of the QCD NL corrections to the gluon-gluon fusion and the VBF processes (Section 3). Great progress has been made in recent years in understanding QCD Next-to-Next-to-Leading- rder effects, QCD NL corrections to other production mechanisms and EW corrections. We do not deem it appropriate to review this question here, instead we refer the reader to a comprehensive review [43].

[9] Cross-sections were computed with [34].

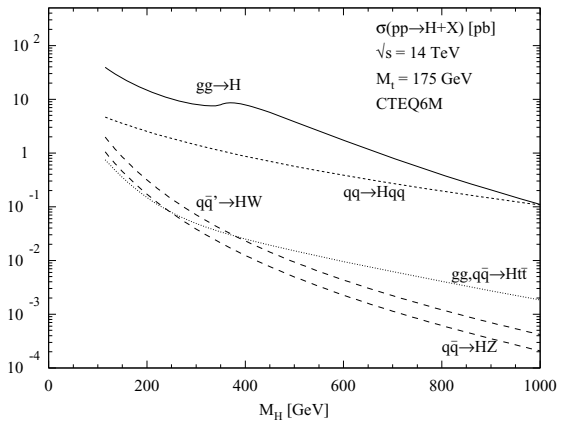

Figure 8. Production cross-section for the SM Higgs boson in proton proton collisions with the centre of mass of the LHC. Results are given for different production mechanisms as a function of the mass (see text)

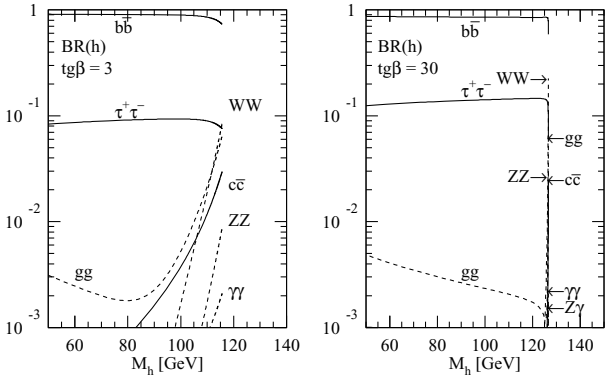

Figure 9. Branching ratio of the MSSM Higgs boson h to different decay products as a function of the mass. Results are given for two regions in the MSSM parameter space, $\tan\beta = 3, 30$

top-quark alongside the Higgs, or high-p_T high-η jets from VBF, allow for triggering on events with Higgs boson in invisible final states.

Efforts have been developed to understand the sensitivity of the detectors for the minimal expression of the Higgs boson sector, a single Higgs boson doublet. With the extension of the Higgs boson sector by the addition of a second Higgs boson doublet, the situation becomes more complex, as the multiplicity of relevant final states is enhanced. In the latter case, within the context of the minimal supersymmetric (MSSM) extension, the Higgs boson sector contains two charged ($H^\pm$) and three neutral (h, H, A) physical states.[10] All Higgs boson masses and couplings are expressed in terms of two parameters: the mass of the CP-odd boson, m_A, and the ratio of the vacuum expectation values of the Higgs boson doublets, $\tan\beta$. Here we consider the case when the mass of supersymmetric particles are large enough so that they do not play an important role in the phenomenology. A review of the impact of supersymmetric particles can be found in [44].

Whereas Figures 9-11 show the branching ratio of the MSSM Higgs bosons $h, A, H^\pm$ as a function of the mass, Fig. 12 refers to production cross-section of the MSSM Higgs boson in proton-proton collision. Results are given for two representative points in the MSSM parameter space.

The production processes shown in Fig. 7 for the SM Higgs can also be computed for the CP-even h, H bosons. However, the production mechanism involving the b-quark will play an important role for moderate to large $\tan\beta$ values as the couplings to the Higgs boson are enhanced. Firstly, one has to take into account the b-quark loop contribution in the $gg \to h, H$ mechanism. Secondly, associated Higgs boson production with heavy quarks in the final states must be considered, $pp \to b\bar{b}h, H$ and this process for either h or H becomes the dominant one in the MSSM. The cross sections for the associated production with $t\bar{t}$ pairs and with W/Z bosons as well as the WW/ZZ fusion processes, are suppressed for at least one of the particles as a result of the VV coupling reduction.

Because of CP invariance, which forbids AVV couplings, the A boson cannot be produced in the Higgs-strahlung and VBF processes; the rate for the $pp \to t\bar{t}A$ mechanism is suppressed due to the small $At\bar{t}$ coupling for $\tan\beta > 3$. The processes $gg \to A$, including the b-quark loop and the production in association with $b\bar{b}$ pairs yield significant cross-sections. The one-loop induced diagrams $gg \to AZ, Ag$ and the associated production with other Higgs bosons are possible but their cross-sections are typically small.

Concerning the production of the charged Higgs boson, it is important to consider the mass. For Higgs boson masses lighter than the top-quark mass, the dominant channel is the production from top-quark decays. For higher masses, one needs to consider the processes

[10] It is relevant to note that the notation for a SM Higgs boson is H, where the notation for the lightest and heaviest neutral CP-even MSSM Higgs boson is h, H, respectively.

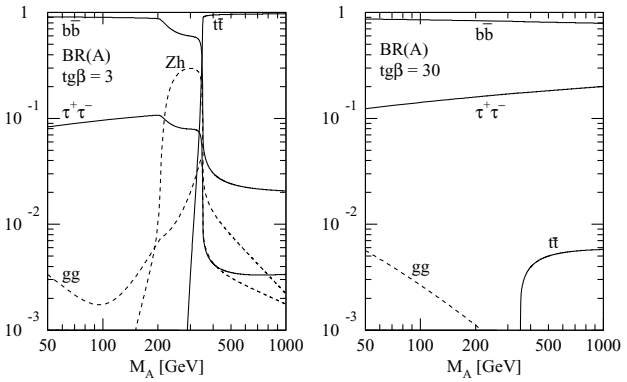

Figure 10. Branching ratio of the MSSM Higgs boson A to different decay products as a function of the mass. Results are given for two regions in the MSSM parameter space, $\tan\beta = 3, 30$

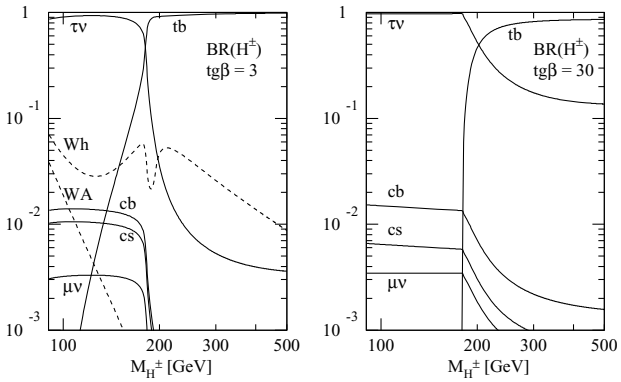

Figure 11. Branching ratio of the MSSM Higgs boson $H^{\pm}$ to different decay products as a function of the mass. Results are given for two regions in the MSSM parameter space, $\tan\beta = 3, 30$

$gg \to H^{\pm}tb$ and $gb \to H^{\pm}t$, which have to be properly combined in order to compute the physical cross-section.

A comprehensive review of the properties and the production mechanism of the MSSM Higgs bosons can be fond in [44]. A brief discussion on the sensitivity for these experiments to discover one or more of the Higgs bosons from the minimal version of the supersymmetric theories is also included (Section 4).

3.2. Experimental Reconstruction of Physics Objects

Here we briefly review the experimental reconstruction of physics objects that are relevant to the search of the Higgs boson with the CMS and ATLAS detectors. As seen in section 3.1 the search for the Higgs boson will involved a variety of final states. This will include the reconstruction of photons, electrons, muons, hadronic τ decays, hadronic jet reconstruction, b-jet reconstruction and the computation of missing transverse momentum, $\not{p}_T$, carried by neutrinos.

Electrons are reconstructed as objects that have a track in the Inner Tracker and an electromagnetic cluster in the electromagnetic section of the calorimeter. In order to separate isolated electrons originating from interesting events, from QCD background (hadrons, jets and photons) with similar topology, several of their characteristics are exploited. The electro-magnetic cluster in the calorimeter is required to match with a track in the Inner Tracker and the ratio of its energy over its momentum measured by the tracker (E/p) to be that of an electron. Cuts on the longitudinal (and lateral) shape of the shower are applied, and minimal energy is allowed to be deposited in the hadronic calorimeter. Rejections of $10^4 \div 10^6$ against hadronic jets can be achieved, depending on the definition of the electron identification, transverse momentum and angle.

Photons are also reconstructed as electromagnetic clusters with a different treatment of the information given by the inner detector. For identification purposes photon candidates are classified into unconverted (no high p_T tracks are associated) and converted (one or two high p_T tracks are associated). Due to the large amount of inactive material in front of the face of the calorimeter, a significant fraction of photons will convert into a e^+e^- pair, leading to the observation of one or two tracks, depending on the circumstances of the conversion. Sophisticated tracking algorithms are implemented in order to identify a vertex produced by a e^+e^- pair with a large distance to the beam-line. In addition, single tracks are searched for such that no hits

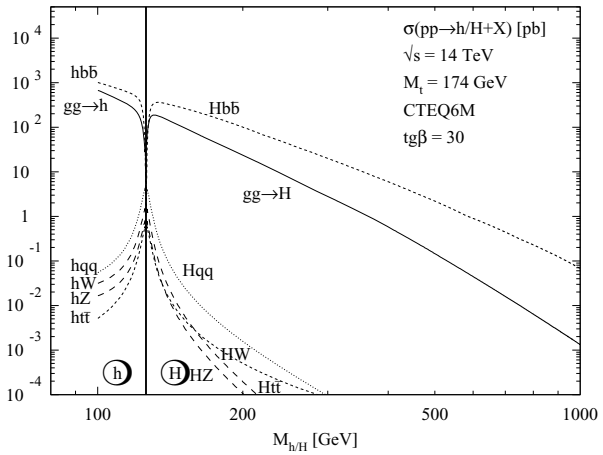

Figure 12. Production cross-section of the MSSM Higgs boson h, H in proton-proton collisions with the centre of mass of the LHC, as a function of the mass. The results are presented for $\tan\beta = 30$

are found in the layer of the silicon detectors closest to the beam-pipe. Rejections of $10^3 \div 10^4$ against hadronic jets can be achieved, depending on the definition of the photon identification, transverse momentum and angle.

The calorimeter is designed to contain almost all of the energy of a high p_T (TeV range) electron/photon, and has an energy resolution of $2 \div 10\%/\sqrt{E[\text{ GeV}]}$, depending on the experiment. The energy resolution for electron and photon candidates is similar.

Muons are reconstructed as objects that have a track in the muon spectrometer and a corresponding ("matched") track in the Inner Tracker. In the case of ATLAS, the good resolution of the muon spectrometer provides the possibility to trigger and reconstruct muons in "stand alone" mode (no matching with the inner detector involved). The momentum resolution is maintained high for both experiments. For low momenta the muon momentum resolution is dominated by the resolution of the Inner Tracker. The Inner Tracker has an intrinsic p_T resolution of a few times $10^{-4} p_T(\text{ TeV}/c)$, which is limited by early bremsstrahlung in its material. For muon p_T in the TeV/c range the resolution is limited by detector alignment in the case of ATLAS and can be kept at $\sigma/p_T \approx 10\%$, whereas in the case of CMS it is limited by energy losses in the iron yoke, and it varies between $15 \div 30\%$.

For the reconstruction of hadronic jets, a seeded fixed-cone reconstruction algorithm with a cone size $\Delta R = \sqrt{\Delta\phi^2 + \Delta\eta^2} = 0.4$ is presently used for search studies the Higgs boson. For future studies also the SISCone (Seedless Infrared Safe Cone) jet algorithm and the fast K_T algorithm are considered. If one neglects the noise term, the jet energy resolution varies between $50 \div 100\%/\sqrt{E[\text{ GeV}]}$, depending on the angle and the detector. Both experiments have strong capabilities for the identification of b-jets and τ-jets in wide range of transverse momentum for $|\eta| < 2.5$. For a b-jet tagging efficiency of 60% and transverse momentum of $20 < p_T < 100$ GeV/c a rejection above 100 and about 10 may be achieved against light an c-jets, respectively, with degradation of performance for $p_T > 100$ GeV/c. For a τ-jet efficiency of 50%, the rejection against hadronic jets improves with p_T, reaching rejection values of $(10^2) \div (10^3)$.

The missing transverse momentum carried by neutrinos is primarily reconstructed from the energy deposits in the calorimeter and the reconstructed muon tracks. Apart from the hard scattering process of interest, many other sources, such as the underlying event, multiple interactions, pileup and electronic noise lead to energy deposits and/or fake muon tracks. Classifying these energy deposits into various types (e.g. electrons, taus or jets) and calibrating them accordingly, is the essential key for optimal $\not{p}_T$ measurement. In addition, the loss of energy in regions of inactive material and dead detector channels make the $\not{p}_T$ measurement a real challenge.

The $\not{p}_T$ reconstruction algorithm starts from the energy deposits in calorimeter cells or clusters of cells ("raw $\not{p}_T$"). The raw $\not{p}_T$ is then cleaned up from a number of sources of fake $\not{p}_T$: hot cells, overlay of beam-halo, cosmics, detector malfunctions, detector hermiticity. Overall, the reconstruction of $\not{p}_T$ is a challenging task and it requires a good understanding of the calorimeter response and the topology of different signatures. The $\not{p}_T$ resolution roughly scales with $\sqrt{\sum E_T}$, where $\sum E_T$ is the scalar sum of the energies of the particles in the final state, for $\sqrt{\sum E_T} <$ 1.5 TeV.

Both CMS and ATLAS have conducted extensive fully-simulated GEANT-based [45] Monte Carlo studies to determine the experimental viability of all of these channels. A few of these signatures are highlighted below. A more comprehensive and complete account can be found elsewhere [16, 17, 23].

3.3. Discovery Channels

In this section we succinctly put in perspective the relevant theoretical inputs (Section 3.1) and corresponding experimental parameters (Section 3.2) needed to define the strategy for the observation of the Higgs boson.

Analysis	$\gamma\gamma$	$\tau\tau$	WW	ZZ
Inclusive	Yes	NA	Yes	Yes
≥ 1 jet	Yes	Yes	Yes	NA
≥ 2 jet	Yes	Yes	Yes	NA
Z/WH	Yes	NA	Yes	NA
$t\bar{t}H$	Yes	NA	Yes	NA

Table 1. Final states with the potential to give a significant contribution to the discovery of the SM Higgs boson at the LHC. The those final states labeled as NA correspond to channels that are not feasible or for which feasibility studies are not available.

Table 1 summarises the final states with the potential to give a significant contribution to the discovery of the SM Higgs boson at the LHC. Those final states labeled as NA correspond to channels that are not feasible or for which feasibility studies (for discovery purposes) are not available. Below we give a summary of the most relevant aspects of the experimental analysis involving $H \to \gamma\gamma, \tau\tau, WW, ZZ$ decays.

The feasibility of channels intrinsic to the observation of MSSM Higgs bosons will be also briefly discussed in section 4. This includes the search for di-μ and di-τ pairs. The feasibility of these searches is usually performed when the di-μ and di-τ pairs are produced in association with at least one b-jet.[11] The potential of the decay chains, such as $Wh \to l\nu b\bar{b}$ ($l = e, \mu$), $A/H \to t\bar{t}$, $A \to Zh \to llb\bar{b}$ ($l = e, \mu$) and $H \to hh \to b\bar{b}\gamma\gamma$ has been evaluated. The decay mode $H^{\pm} \to \tau^{\pm}\nu$ is considered, as well.

3.3.1. $\mathbf{H \to \gamma\gamma}$

Despite the small branching ratio, $H \to \gamma\gamma$ remains a very attractive channel for $115 < M_H < 140$ GeV/c^2. The feasibility of this channel heavily relies on excellent photon resolution due to the small signal to ratio expected for the inclusive analysis. In addition to the required calorimeter resolution, the reconstruction of the di-photon vertex plays a significant role. This is achieved by using the main vertex of the event produced by the multiplicity of low p_T tracks (the underlying event) and hadronic jets.

The backgrounds to this channel are usually divided into two types: irreducible and reducible. Photon pairs from $^{-} \to \gamma\gamma$, $gg \to \gamma\gamma$ and quasi-collinear quark bremsstrahlung comprise the irreducible background, while jet-jet and γ-jet events, where one or more jets are misidentified as photons (mostly from the production of energetic π^0s), take up the bulk of the reducible background. $Z \to e^+e^-$ events, with both electrons misidentified as photons, can be reduced using electron/photon separation techniques. Excellent photon identification is required in order to suppress the reducible backgrounds, and, in particular, to separate π^0s leading to two collimated photons from a single photon. The high-granularity Liquid Argon calorimeter of ATLAS is capable of resolving single photons from π^0s,[12] while CMS has a superior energy resolution.[13]

Studies conducted of the inclusive analysis by both experiments consider the signal and backgrounds to QCD NLO [46–52]. Both experiments have looked beyond a simple cut-based analysis. The discriminating power of the di-photon transverse momentum and the photon decay angle in the Higgs boson rest frame with respect to the Higgs boson lab flight direction, $|\cos\theta^*|$, are evaluated in conjunction with the di-photon invariant mass.

Efforts have been made to evaluate the feasibility of Higgs boson searches in association with at least one or two high p_T hadronic jets. The sensitivity of the Higgs boson production in association with Z, W and $t\bar{t}$ has also been evaluated.

The sensitivity of this channel is similar for both experiments. For $M_H = 130$ GeV/c^2, and an integrated luminosity of 30 fb^{-1} of integrated luminosity more than a $5\,\sigma$ effect may be achieved with one experiment, as illustrated in Fig. 13. The sensitivity of this channel can increase significantly with a more sophisticated treatment of discriminating variables. This is illustrated in Fig. 13, where the sensitivity of the cut-based analysis is compared to that of a more complete analysis.

3.3.2. $\mathbf{H \to \tau\tau}$

As pointed out in Table 1, the search for a SM Higgs boson with the $H \to \tau\tau$ decay requires the presence of at least one high p_T jet.[14] The final state with at least two high p_T jets is the best studied by the CMS and ATLAS collaborations. The distinct experimental signature of Higgs boson production via VBF, with jets from the "struck quarks" at high-η and Higgs boson

[11] The feasibility of purely inclusive searches using $A/H \to \mu\mu, \tau\tau$ at the LHC is being evaluated.

[12] The ATLAS calorimeter is able to suppress π^0s by a factor of $2.5 \div 3$ in the range of transverse momentum relevant to the SM Higgs boson search [28].

[13] Detailed comparisons of the sensitivity of the two experiments are underway.

[14] The inclusive search for excess of events di-τ pairs carries sensitivity to the MSSM light h for large values of $\tan\beta$.

decay products in the central region is a great asset for channels like $H \to \tau\tau$. CMS and ATLAS now both consider three final states, thus covering all combinations of leptonically- and hadronically-decaying taus.[15] Triggering on the fully hadronic mode by using combinations of low-p_T tau and other triggers (e.g. missing transverse momentum or forward jets) are currently under investigation. Despite the presence of multiple neutrinos in the final-state, mass reconstruction can typically be done via the collinear approximation where the tau decay daughters are assumed to be in the same direction as their parent. The reconstruction of the di-τ invariant mass using the collinear approximation is feasible when the τs are not back-to-back, which is the case considered here. The resolution on the reconstructed mass ($\sim$10 GeV/c^2 for $M_H = 120$ GeV/c^2) is mainly affected by the missing energy resolution. Other experimental issues, such as the identification of hadronic taus and low p_T electrons and muons, together with the reconstruction of forward jets and the understanding of the central jet veto are central to the analysis, as well. Data-driven methods for understanding the dominant backgrounds (Z + jets, QCD and $t\bar{t}$) have been investigated. With the combination of all the decay modes, one experiment may achieve $5\,\sigma$ significance for 30 fb^{-1} of integrated luminosity (Fig. 13).

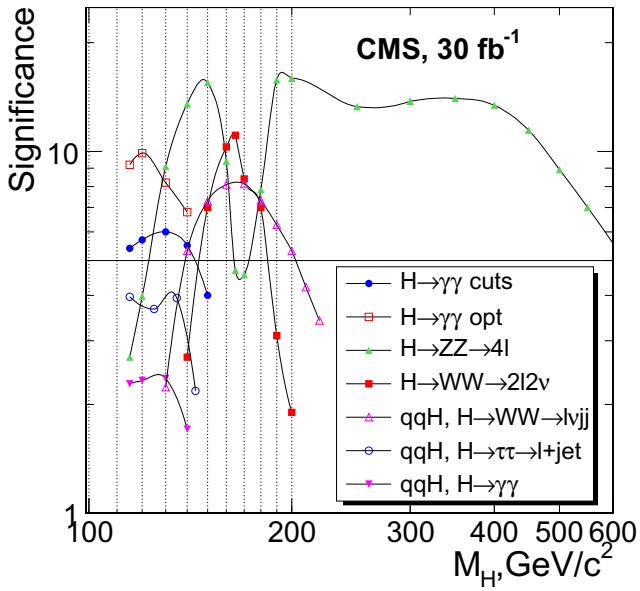

Figure 13. The discovery potential at CMS for SM Higgs boson searches, as obtained using NLO cross-sections, for 30 fb^{-1} of integrated luminosity

3.3.3. $\mathbf{H \to ZZ^{(*)} \to 4l}$ ($\mathbf{4e}$, $\mathbf{4\mu}$, $\mathbf{2e2\mu}$)

At $M_H > 130$ GeV/c^2, the 4-lepton channels gain in importance on account of the energy reconstruction and identification of both ATLAS and CMS for electrons and muons. This analysis is performed inclusively due to the small cross-section of the expected SM backgrounds giving four isolated leptons (e, μ).[16] The dominant backgrounds for these channels are $ZZ^{(*)}$, $Zb\bar{b}$ and $t\bar{t}$ production. Through the use of impact parameter and lepton isolation requirements the latter two can be significantly reduced. The $^{-}$ component of the $ZZ^{(*)}$ background is known at NLO [54–57], however due to the lack of a Monte Carlo generator for $gg \to ZZ^{(*)}$, typically the contribution from this process is added as 30% of the LO $^{-} \to ZZ^{(*)}$.[17] After the imposition of an appropriate event selection the contribution of the reducible $Zb\bar{b}$ and $t\bar{t}$ backgrounds becomes negligible for searches of a heavy Higgs boson and become significantly smaller than the contribution of reducible backgrounds for low mass Higgs boson searches. Collectively, the significance for these channels is more than 5σ for 30 fb^{-1} of integrated luminosity in a wide range of Higgs boson masses (Fig. 13).[18]

3.3.4. $\mathbf{H \to WW^{(*)} \to l\nu l\nu}$ ($\mathbf{l = e,\ \mu}$)

As the branching ratio for a SM Higgs boson decaying to WW is more than 95% at $\sim$ 160 GeV/c^2, this is the most significant channel at that mass point. Unlike other channels, in the $H \to WW \to l\nu l\nu$ final state full mass reconstruction is not possible and the analysis is essentially reduced to a counting experiment; therefore an accurate background estimate is critical. The dominant backgrounds for this analysis are W^+W^- and $t\bar{t}$ production. The former can be suppressed by exploiting spin correlations between the two leptons while the latter has been shown to be suppressed significantly by a jet veto. The CMS and ATLAS collaborations have extensively studied two regimes: an analysis based on

[15] The search for a low mass SM Higgs boson when both τs decay hadronically has been investigated rendering the analysis challenging. Searches for di-τ pairs are feasible when dealing with heavy MSSM Higgs bosons.

[16] The impact of the search for ZZ pairs in association with jets is still being assessed by the collaborations. The isolation of ZZ pairs in conjunction with two high p_T and well separated jets has been addressed within the context of Higgs boson coupling measurements [53].

[17] Currently, the `gg2ZZ` generator is being used in order to properly take into account the $gg \to ZZ^{(*)}$ process, including Z/γ interference effects [58].

[18] The sensitivity of this channel is very strong with the exemption of a narrow window $160 < M_H < 175$ GeV/c^2, where branching ratio of $H \to ZZ$ is diminished (Fig. 6).

the application of a full jet veto[19] and with the tagging of two high p_T hadronic jets.[20] The feasibility of search for WW pairs in association with Z/W and $t\bar{t}$ has been evaluated.

Using NLO [55–57, 59, 60] cross-sections and conservative estimates for the effect of systematic uncertainties, a significance of around 5σ for $M_H = 165$ GeV/c^2 using an integrated luminosity of $\sim$1 fb^{-1} is estimated. The sensitivity of this channel is also evaluated for other Higgs boson masses showing strong sensitivity for the mass range $140 < M_H < 190$ GeV/c^2, as illustrated in Fig. 13.

4. Summary of Higgs Boson Discovery Potential

The expected significance in 30 fb^{-1} of integrated luminosity, for various final states as a function of SM Higgs boson mass is summarised in Fig. 13 for the CMS experiment. The discovery potential at CMS and ATLAS is quite similar. When combining all the most important channels one experiment is expected to reach a $5\,\sigma$ effect in the entire SM Higgs boson mass range of interest with about 10 fb^{-1} of integrated luminosity.

Discovery prospects for the detection of MSSM Higgses (A, h, H and $H^{\pm}$) have also been evaluated [16,17]. At tree-level, all Higgs boson masses and couplings can be expressed in terms of m_A and $\tan\beta$. The complete region of the m_A–$\tan\beta$ parameter space (m_A = 50–500 GeV/c^2 and $\tan\beta$ = 1–50) should be accessible to the LHC experiments. The sensitivity for the discovery of MSSM Higgses, in the minimal mixing scenario for 30 fb^{-1} of data, is summarised in Fig. 14 for the ATLAS experiment. With the further increase of the integrated luminosity the sensitivity the ability to observe more than one Higgs boson for intermediate $\tan\beta$ and large M_A is enhanced. However, there wil always remain a region at intermediate $\tan\beta$ and $M_A > 200 \div 250$ GeV/c^2 for which the observation of more than one Higgs boson will not be feasible. As in the case of the SM Higgs boson, the discovery potential at CMS and ATLAS is quite similar.

Acknowledgments: I would like to whole heartedly thank Prof. Biswarup Mukhopadhyaya and Prof. Amitava Raychaudhuri for the encouragement and strong support. I would also like to thank Prof. Sau Lan Wu, Prof. W. Smith, Prof. S. Dasu, Dr. D. Loveless, Dr. M. Spira, Dr. A. Nikitenko, Dr. W. Quayle, Dr. T. Vickey, Dr. Y. Fang and Dr. X. Chen for their invaluable help in the preparation of the manuscript.

This work was supported in part by the Department of Energy through Grant No. DE-FG0295-ER40896 and the University of Wisconsin Alumni Research Foundation.

[19] Events are rejected in which a hadronic jet is found with $p_T > 20$ GeV/c (hadron level) in the pseudorapidity range $|\eta| < 4.9$. With this selection the leading background is the non-resonant production of W^+W^-.

[20] This analysis is designed to isolate the VBF signal. The leading background is the $t\bar{t}$ production.

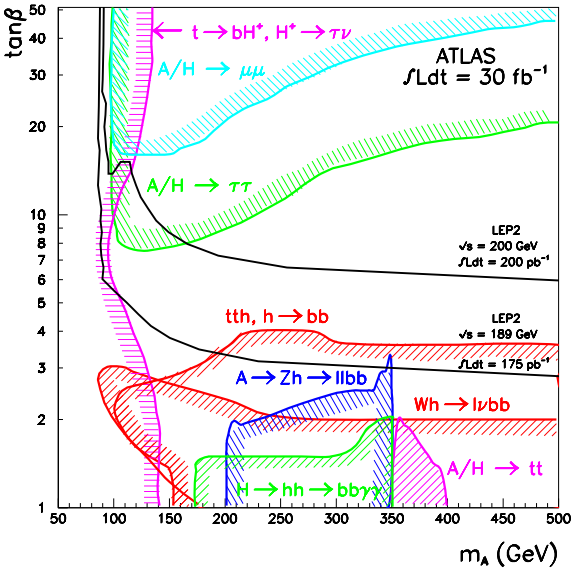

Figure 14. The discovery potential at ATLAS for MSSM Higgs boson searches, for 30 fb^{-1} of integrated luminosity

REFERENCES

1. S. L. Glashow, Nucl. Phys. **22** 1961 579 .
2. S. Weinberg, Phys. Rev. Lett. **19** 1967 1264.
3. A. Salam, Proceedings to the Eigth Nobel Symposium, May 1968, ed N. Svartholm Wiley, 1968 357.
4. S.L. Glashow, J. Iliopoulos and L. Maiani, Phys. Rev. **D2** 1970 1285.
5. F. Englert, R. rout, Phys. Rev. Lett. **13** 1964 321.
6. P. W. Higgs, Phys. Lett. **12** 1964 132.
7. P. W. Higgs, Phys. Rev. Lett. **13** 1964 508.
8. P. W. Higgs, Phys. Rev. **145** 1966 1156.
9. G. S. Guralnik, C.R. Hagen and T.W. . ibble, Phys. Rev. Lett. **13** 1964 585.
10. T.W. . ibble, Phys. Rev. **155** 1967 1554.
11. ALEPH Collaboration, R. arate *et al.*, Phys. Lett. **B495** 2000 1.
12. P. McNamara and Sau Lan Wu, Higgs Particle in the Standard Model Experimental Results from LEP, Reports on Progress in Physics **65** 2002 465.
13. L. Evans and P. ryant editors , LHC Machine, 2008 JINST **3** S08001 2008 .

14. The LEP Higgs Working Group, Phys. Lett. **B565** –2003– 61.
15. The LEP Electroweak Working Group, http–//lepewwg.web.cern.ch/.
16. CMS Collaboration, CMS PTDR – .2– Physics Performance, CERN/LHCC 2006-021.
17. ATLAS Collaboration, Detector and Physics Performance Technical Design Report, CERN-LHCC/99-14/15 –1999–.
18. – . Hagiwara, D.L. Rainwater and D. –eppenfeld, Phys. Rev. **D59** –1999– 014037.
19. T. Plehn, D.L. Rainwater and D. –eppenfeld, Phys. Rev. **D61** –2000– 093005.
20. S. Abdullin *et al.*, Phys. Lett. **B431** –1998– 410.
21. D.L. Rainwater and D. –eppenfeld, Phys. Rev. **D60** –1999– 113004.
22. N. – auer, T. Plehn, D.L. Rainwater and D. –eppenfeld, Phys. Lett. **B503** –2001– 113.
23. S. Asai *et al.*, Eur. Phys. J. C 32 –2004– s19-s54.
24. – . Mellado, W. – uayle and Sau Lan Wu, Phys. Lett. **B611** –2005– 60.
25. – . Mellado, W. – uayle and Sau Lan Wu, Phys. Rev. **D76** –2007– 093007.
26. R.N. Cahn, S.D. Ellis, R. – leiss and W.J. Stirling, Phys. Rev. **D35** –1987– 1626.
27. The CMS Collaboration, S. Chatrchyan *et al*, The CMS experiment at the CERN LHC, 2008 JINST **3** S08004.
28. The ATLAS Collaboration, G. Aad *et al*, The ATLAS experiment at the CERN Large Hadron Collider, 2008 JINST **3** S08003.
29. The LHCb Collaboration, A.A. Alves Jr *et al*, The LHCb Detector at the LHC, 2008 JINST **3** S08005.
30. The TOTEM Collaboration, G. Anelli *et al*, The TOTEM Experiment at the CERN Large Hadron Collider, 2008 JINST **3** S08007.
31. The ALICE Collaboration, – . Aamodt *et al*, The ALICE experiment at the CERN LHC, 2008 JINST **3** S08002.
32. ATLAS Collaboration, ATLAS Level-1 Trigger– Technical Design Report, CERN-LHCC-98-014, ATLAS-TDR-12 –1998–.
33. ATLAS Collaboration, High-Level Trigger Data Ac–uisition and Controls, CERN-LHCC-03-016, ATLAS-TDR16 –2003–.
34. A. Djouadi, J. – alinowski and M. Spira, HDECA– – a Program for Higgs – oson Decays in the Standard Model and its Supersymmetric Extention, Comp. Phys. Comm. **108** –1998– 56.
35. H.M. Georgi, S.L. Glashow, M.E. Machacek and D.– . Nanopoulos, Phys. Rev. Lett. **40** –1978– 692.
36. R. Cahn and S. Dawson, Phys. Lett. **B136** –1984– 196.
37. G. – ane, W. Repko and W. Rolnick, Phys. Lett. **B148** –1984– 367.
38. S. Dawson, Nucl. Phys. **B359** –1991– 283.
39. A. Djouadi, M. Spira and P.M. –erwas, Phys. Lett. **B264** –1991– 440.
40. D. Grauden–, M. Spira and P.M. –erwas, Phys. Rev. Lett. **70** –1993– 1372.
41. M. Spira, A. Djouadi, D. Grauden– and P.M. –erwas, Nucl. Phys. **B453** –1995– 17.
42. T. Han, G. – alencia and S. Willenbrock, Phys. Rev. Lett. **69** –1992– 3274.
43. A. Djouadi, Phys. Rep. **457** –2008– 1.
44. A. Djouadi, Phys. Rep. **459** –2008– 1.
45. S. Agostinelli et al., NIM A **506** –2003– 250–303.
46. T. – inoth *et al.*, E. Phys. J. **C16** –2000– 311.
47. C. – ala–s, E. – erger, S. Mrenna and C.-P. – uan, Phys. Rev. **D57** –1998– 6934.
48. C. – ala–s, E. – erger, P. Nadolsky, C. Schmidt and C.-P. – uan, Phys. Lett. **B489** –2000– 157.
49. C. – ala–s, E. – erger, P. Nadolsky and C.-P. – uan, Phys. Lett. **B637** –2006– 235.
50. S. Catani, M. Fontanna–, J.P. Guillet, and E. Pilon, JHEP **05** –2002– 028.
51. –. Nagy, Phys. Rev. Lett. **88** –2002– 122003.
52. –. Nagy, Phys. Rev. **D68** –2003– 094002.
53. M. Duhrssen *et al.*, Phys. Rev. **D70** –2004– 113009.
54. – . Mele, P. Nason and G. Ridolfi, Nucl. Phys. **B357** –1991– 409.
55. J. Ohnemus, Phys. Rev. **B50** –1994– 1931.
56. J. Campbell, R.– . Ellis, Phys. Rev. **D60** –1999– 113006.
57. S. Frixione and – .R. Webber, JHEP **0206** –2002– 029.
58. T. – inoth, N. – auer and P. Mertsch, Gluon-induced – CD corrections to $pp \to ZZ \to l\bar{l}l'\overline{l'}$, To appear in the proceedings of 16th International Workshop on Deep Inelastic Scattering and Related Subjects –DIS 2008–, London, England, 7-11 Apr 2008. e-Print–ar– iv–0807.0024 –hep-ph–.
59. J. Ohnemus, Phys. Rev. **B44** –1991– 1403.
60. S. Frixione, Nucl. Phys. **B410** –1993– 280.